

## REMARKS

Applicant intends this response to be a complete response to the Examiner's **7 May 2009** Non-Final Office Action. Applicant has labeled the paragraphs in his response to correspond to the paragraph labeling in the Office Action for the convenience of the Examiner.

### DETAILED ACTION

#### *Continued Examination Under 37 CFR 1.114*

The Examiner states as follows:

1. A request for continued examination under 37 CFR 1.114, including the fee set forth in 37 CFR 1.17(e), was filed in this application after final rejection. Since this application is eligible for continued examination under 37 CFR 1.114, and the fee set forth in 37 CFR 1.17(e) has been timely paid, the finality of the previous Office action has been withdrawn pursuant to 37 CFR 1.114. Applicant's submission filed on March 23,2009 has been entered.

Applicants acknowledge the Examiner's statements.

#### *Response to Amendment and Arguments*

The Examiner states as follows:

2. Applicant's amendment filed on March 23,2009 has been entered and made of record.

Applicants acknowledge the Examiner's statements.

#### *Requirement for Information under 37 CFR 1.105*

The Examiner states as follows:

3. Applicant and the assignee of this application are required under 37 CFR 1.105 to provide the following information that the examiner has determined is reasonably necessary to the examination of this application.

In response to this requirement, please provide a copy of the article "Nonseparable bidimensional wavelet bases" by Cohen et al., which was cited in the article "Non-separable Radial Frame Multiresolution Analysis in Multidimensions and Isotropic Fast Wavelet Algorithms" by Papadakis et al. In addition, please provide a concise explanation of the reliance placed on that publication in the development of the disclosed subject matter.

Applicants points out to the Examiner that most of the cited references are not relevant to the invention, but merely direct the reader to where certain mathematic derivations and/or functions are described or where certain mathematical understandings can be found and where certain understandings about human vision can be found. The following list of references and there specific usage in the specification are set forth below:

[6] J.J. Benedetto and S. Li. The Theory of Multiresolution Analysis Frames and Applications to Filter Banks. *Appl. Comp. Harm. Anal.*, 5:389-427, 1998, *deal with filters that can be constructed from the filters of this invention.*

[7] A. Cohen and I. Daubechies. Nonseparable Bidimensional Wavelet Bases. *Revista Matematica Iberoamericana*, 9:51-137, 1993; [12] J. Kovacevic and M. Vetterli. Nonseparable Multidimensional Perfect Reconstruction Filter-banks. *IEEE Transactions on Information Theory*, 38:533-555, 1992; [11] W. He and M.J. Lai. Examples of Bivariate Nonseparable Compactly Supported Orthonormal Continuous Wavelets. In M. Unser, A. Aldroubi, A. Laine editor, *Wavelet Applications in Signal and Image Processing IV*, volume 3169 of *Proceedings SPIE*, pages 303-314, 1997; [8] K. Grochenig and W. Madych. Multiresolution Analysis, Haar Bases and Self-Similar Tilings. *IEEE Transactions on Information Theory*, 38:558-568, 1992; [4] A. Ayache, E. Belogay, and Y. Wang. Orthogonal Lifting: Constructing New (Symmetric) Orthogonal Scaling Functions. 2002; [5] E. Belogay and Y. Wang. Arbitrarily Smooth Orthogonal Nonseparable Wavelets in  $\mathbb{R}^2$ . *SIAM Journal of Mathematical Analysis*, 30:678-697, 1999; [1] E.H. Adelson, E. Simoncelli, and R. Hingorani. Orthogonal Pyramid Transforms for Image Coding. In *Visual Communications and Image Processing II*, Volume 845 of *Proceedings SPIE*, pages 50-58, 1987; [18] E.P. Simoncelli, W.T. Freeman, E.H. Adelson, and J.P. Hager. Shiftable Multi-Scale Transforms. *IEEE Transactions Information Theory*, 38(2):587-607, 1992; and [19] J. Starck, E. J. Candes, and D.L. Donoho. The Curvelet Transform for Image Denoising. *IEEE Transactions Image Processing*, 11(6):670-684, 2002), *all dealing with different construction for performing multi-resolution analysis. Of note are the references of quincunx filtering schemes for performing multi-resolution analysis, which are stated in the specification as having "some continuity properties with respect to dyadic dilations or dilations induced by the Quincunx matrix only have been constructed in the past. All of them have no axial symmetries and are not smooth, except those constructed in E. Belogay and Y. Wang. Arbitrarily Smooth Orthogonal Nonseparable Wavelets in  $\mathbb{R}^2$ . SIAM Journal of Mathematical Analysis*, 30:678-697, 1999, which can be made arbitrarily smooth, but are highly asymmetric."

[20] M. Vetterli and J. Kovacevic. *Wavelets and Subband Coding*. Prentice Hall PTR, Englewood Cliffs, NJ, 1995; [13] D. Marr. *Vision, A Computational Investigation into the Human Representation and Processing of Visual Information*. W. H. Freeman and Co., New York, N.Y., 1982; and [14] D. Marr and E. Hildreth. The Theory of Edge Detection. *Proc. R. Soc. London B*, 207:187-217, 1980, *deals with the fact that the human visual system critically depends on edge detection and with a specific construct to formula Laplacian filters to mimic the human visual system.*

[9] D. Han, D.R. Larson, M. Papadakis, and T. Stavropoulos. Multiresolution Analysis of Abstract Hilbert Spaces and Wandering Subspaces. In D. R. Larson L. Baggett, editor, *The Functional and Harmonic Analysis of Wavelets and Frames*, volume 247 of *Cont. Math.*, pages 259-284. Amer. Math. Soc., 1999, *relates to a proof that  $\sigma$  is an injective homomorphism and  $\sigma(G)$  is a subgroup of  $G$ .*

[17] M. Pinsky. *An Introduction to Fourier Analysis and Wavelets*. 2001, *relates to the proof of equation (7), which can be found in Lemma 2.5.1 of Pinsky.*

[17] M. Pinsky. *An Introduction to Fourier Analysis and Wavelets*. 2001; [3] G.E. Andrews, R. Askey, and R Roy. *Special Functions*. Number 71 in *Encyclopedia of Mathematics*. Cambridge University Press, 2000; and [21] G.N. Watson. *A Treatise on the Theory of Bessel Functions*. Cambridge Mathematical Library. Cambridge University Press, 1944, *relate to details regarding Bessel functions and an extensive treatment of their main properties.*

[2] A. Aldroubi. Portraits of Frames. *Proceeding of the American Mathematical Society*, 123: 1661-1668, 1995 and [10] D. Han and D.R. Larson. *Frames, Bases and Group Representations*, volume 147 of *Memoirs*. American Mathematical Society, 2000, *relate to supporting the statement in the specification that an arbitrary orthogonal projection  $R$  defined on a Hilbert space  $H$  maps every orthonormal basis of  $H$  onto a Parseval frame for  $R(H)$ .*

The text in bold and italics is derived directly from the specification, where each reference was cited and can be found in the following paragraphs: [0031], [0032], [0033], [0041], [0062], [0063], and [0078].

Applicants believe that the two Papadakis references were already submitted to the Examiner,

but these two references form the background from which the method and system of this invention was derived, but in no way disclosed or taught now to go about the construction, which is the purpose of the present invention.

Applicants attach a rule 132 Declaration concerning the Cohen et al. reference, in which Dr. Papakadis declares that the inventors did not rely on the Cohen et al. reference to derive the present invention.

### ***Specification***

The Examiner contends as follows:

4. The specification is objected to because pages 26-27 contain a list of publications cited by the specification. According to the MPEP § 609 A(1) "the list may not be incorporated into the specification but must be submitted in a separate paper." Therefore, Examiner suggests Applicants file a separate information disclosure statement following the requirements of 37 CFR 1.98(b), which requires a list of all patents, publications, or other information submitted for consideration by the Office. The list is improper and thus, must be removed from the specification.

Applicants' attorney has never been required to remove as list of references from an application. Most of the references are not directly relevant to claim inventions of this invention, but they are merely direct readers to additional information about certain mathematical functions, derivations and/or understandings and understanding concerning human visual system. As shown above in the information disclosure statement section, the references are characterized as set forth expressly in the specification. Applicants have moved each reference to the place where it was cited in the specification so that readers can be directed to the articles or books that deal directly with the derivation or understanding being set forth at that location in the specification.

### ***Claim Rejections - 35 USC § 101***

5. **Claims 1-6, 13-24** stand rejected under 35 U.S.C. 101 as not falling within one of the four statutory categories of invention.

The Examiner contends as follows:

Federal Circuit precedent (*In re Bilski*, 88 USPQ2d 1385 (Fed. Cir. 2008)) requires that a statutory "process" under 35 U.S.C. 101 must (1) be tied to another statutory category (such as a particular apparatus), or (2) transform underlying subject matter (such as an article or material) to a different state or thing. While the instant claim(s) recite a series of steps or acts to be performed, the claim(s) neither transform underlying subject matter nor positively tie to another statutory category that accomplishes the claimed method steps, and therefore do not qualify as a statutory process under 35 U.S.C. 101 (Claim 15's recitation of a computer does not make the claim statutory because the computer is recited in the preamble and therefore, not given patentable weight.).

Applicant's amendment to claims 1 and 4, adding the limitation "implemented on a computer" fails to overcome the 101 rejection above because the computer is recited in the preamble and thus, is not given any patentable weight.

Applicants have amended the claims to add that the components are "in the form of software code executable on the computer," which is supported in the specification at least at paragraphs 12 and 27. Applicants also state that the entire specification is directed to the construction of a system of software implemented on a computer designed to transform signals, information, data or images into wavelet decomposed and resolved sub-bands or resolution levels that can then be used to reconstruct a filtered resolution of the signals, information, data or images, which have improved properties and enhanced feature recognition. While the constructs that accomplish the signal, information, data or image transformation are computerized software derived from mathematical expression, the raw signals, information, data or images are not merely translated, scaled, rotated, or moved, but are filtered, decomposed and ultimately reconstructed into transformed signals, information, data or images with improved properties that greatly facilitate analysis. Filtering by definition results in a change in data. The original data is subjected to a set of filtering operation to enhance analysis of the data. In this case, the filtering is performed by completely isotropic, non-separable wavelets that are constructed from completely isotropic, non-separable windows, operations and filters, where the method can be extended to any dimension. Nothing in the prior art discloses or even suggests such a system or method.

6. **Claims 11-12** are rejected under 35 U.S.C. 101 because the claims merely recite mathematical functions.

The Examiner contends as follows:

Although a "computer" is recited in the claim, the recitation of the computer is in the preamble and thus, is not given patentable weight.

Applicants have amended claims 11 and 12 to depend from claim 1 and have amended claim 1 to make it clear that the steps result in software code executable on the computer. Applicants, therefore, respectfully requests withdrawal of this rejection.

7. **Claims 13-14** are further rejected under 35 U.S.C. 101.

The Examiner contends as follows:

The claims are nothing more than a mathematical algorithm. See MPEP 2106.02.

Applicants have amended claims 13 and 14 to depend from claim 1 and have amended claim 1 to make it clear that the steps result in software code executable on the computer. Applicants, therefore, respectfully requests withdrawal of this rejection.

***Claim Rejections - 35 USC § 102***

8. **Claims 7-10** stand rejected under 35 U.S.C. 102(b) as being anticipated by Bouchard et al., U.S. Patent No. 5,898,798 ("Bouchard").

The Examiner contends as follows:

Referring to claim 7, Bouchard discloses a system for processing signals implemented on a computer comprising:

a processing unit having encoded thereon a completely isotropic, non-separable ideal filter for frame multi-resolution analysis software including [col. 4, II, 13-35 and col. 5, II, 57-67];  
wavelets adapted to resolve a multidimensional signal into various resolution levels [col. 3, II, 29-39 and col. 4, II, 13-35], where the wavelets are derived from:  
isotropic, non-separable ideal windows or filters in a dimension greater than 1, isotropic, non-separable low pass filters, isotropic, non-separable high pass filters and isotropic, non-separable filters that cover a desired frequency range or plurality of frequency ranges; and isotropic, non-separable frame scaling functions where translations of the frame scaling functions form a frame [col. 4, II, 13-35. Note the bidimensional non-separable low and high-pass filters and scaling functions that allow the image to be processed in an isotropic way.];

where the system resolves or decomposes multidimensional signals, data, information, or images into a plurality of non-overlapping sub-bands sets or resolution levels with the at least one isotropic, non-separable wavelet improving analysis efficiency and improving analysis of more complex multidimensional signals, data, information or images [col. 3, II, 29-39 and col. 4, II, 13-35].

Quincunx filters are non-separable, but are not isotropic. In fact, Bouchard entire system is built around preparing quincunx filter banks that are bidimensional, but are not isotropic as is clearly shown in Figure 3 and the associated text of Bouchard. Bouchard's bidimensional non-separable low and high-pass filters are bases on a quincunx grid and are rotational invariant for rotation angles of  $\pi/4$ . Bouchard at Col. 4, 13-35. Bouchard designed the bidimensional non-separable low and high-pass filters to accommodate a specific rotational symmetry. While the bidimensional non-separable quincunx wavelets have limited rotational symmetry that is designed into the wavelets when they are formed, **the bidimensional non-separable quincunx wavelets are not isotropic**. While it is true that quincunx wavelets can be designed to be nearly isotropic, they are not isotropic (see M. Feilner, D.V. De Ville, and M. Unser, "An Orthogonal Family of Quincunx Wavelets With Continuously Adjustable Order," IEEE TRANSACTIONS ON IMAGE PROCESSING, VOL. 14,

NO. 4, APRIL 2005 attached). Applicants also directly and expressly address quincunx wavelets in specification stating:

[0032] In this invention, we construct non-separable Shannon-like GFMRAs of  $L^2(\mathbb{R}^n)$  whose scaling functions are radial and are defined with respect to certain unitary systems, which we will later introduce. We also derive certain of their associated frame multiwavelet sets. Our construction is the first of its kind. Scaling functions that are radial have not been constructed in the past. However, certain classes of non separable scaling functions in two dimensions, with some continuity properties with respect to dyadic dilations or dilations induced by the Quincunx matrix only have been constructed in the past (e.g., [7, 12, 11, 8], [4]). All of them have no axial symmetries and are not smooth, except those constructed in [5], which can be made arbitrarily smooth, but are highly asymmetric. Another construction in the spirit of digital filter design, but not directly related to wavelets can be found in [1] and [18]. The latter construction and this of curvelets (e.g., see [19]) share two properties of our Radial GFMRAs: the separability of the designed filters with respect to polar coordinates and the redundancy of the induced representations. However, our construction in contrast to those due to Simoncelli et. al. and to Starck et al. are in the spirit of classical multiresolution analysis and can be carried out to any number of dimensions and with respect to a variety of dilation matrices.

Specification at Paragraph [0032] (emphasis added).

The present invention relates to wavelets that are isotropic, not nearly so.

Moreover, quincunx wavelets and quincunx multi resolution analysis is limited to 2 dimensions only and is not extendable to 3 or more dimension, save for accumulating a set of 2D slices of a 3D image, where each 2D slice is analyzed using a quincunx formalism (see D.V. De Ville, Thierry Blu, and Michael Unser, "On the Multidimensional Extension of the Quincunx Subsampling Matrix," IEEE SIGNAL PROCESSING LETTERS, VOL. 12, NO. 2, FEBRUARY 2005 attached). The present invention utilized completely isotropic, non-separable windows, operators, filters and wavelets to perform multiresolution analysis without any dimensional constraints.

Because Bouchard does not disclose or teach **completely isotropic**, non-separable windows, operators, filter and wavelets of this invention, Bouchard cannot anticipate claim 7 as claim 7 relates specifically to a system based on completely isotropic, non-separable windows, operators, filter and wavelets. Moreover, Bouchard does not even suggestion or directly an ordinary artisan to function that are completely isotropic and non-separable as Bouchard is tied to quincunx bidimensional wavelets. Applicants, therefore, respectfully request withdrawal of this rejection.

The Examiner contends as follows:

Referring to claims 8-10, Bouchard further discloses that each isotropic, non-separable high pass and each isotropic, non-separable low pass filter comprise: a plurality of isotropic, nonseparable high pass and isotropic, non-separable low pass components, each component including at least one isotropic,

non-separable relative low pass subcomponent and at least one isotropic, non-separable relative high pass subcomponent [col. 4, II, 13-35 and fig. 3].

Applicants reassert their argument concerning Bouchard here. Bouchard does not disclose isotropic, non-separable high pass and low pass filters, especially filters constructed from isotropic components. The Bouchard filters are rotational invariant with respect to a specific angle meaning that they will have a directional bias and the Bouchard filters are imitated to 2D analysis. The present invention utilizes completely isotropic windows, operators, filters and wavelets to decompose or resolve signal or image into subbands without regard to the nature of the image as the windows, operators, filters and wavelets are all isotropic. The present system then reconstructs an filtered and enhanced image from the decomposition.

Because Bouchard does not disclose or teach **completely isotropic**, non-separable windows, operators, filter and wavelets of this invention, Bouchard cannot anticipate claim 7 as claim 7 relates specifically to a system based on completely isotropic, non-separable windows, operators, filter and wavelets. Moreover, Bouchard does not even suggestion or directly an ordinary artisan to function that are completely isotropic and non-separable as Bouchard is tied to quincunx bidimensional wavelets. Applicants, therefore, respectfully request withdrawal of this rejection.

Having fully responded to the Examiner's Non-Final Office Action, Applicants respectfully urge that this application be passed onto allowance.

If it would be of assistance in resolving any issues in this application, the Examiner is kindly invited to contact applicant's attorney Robert W. Strozier at 713.977.7000

**The Commissioner is authorized to charge or credit Deposit Account 501518 for any additional fees or overpayments.**

Date: 8 September 2009

Respectfully submitted,

/Robert W. Strozier/

Robert W. Strozier, Reg. No. 34,024

# An Orthogonal Family of Quincunx Wavelets With Continuously Adjustable Order

Manuela Feilner, Dimitri Van De Ville, *Member, IEEE*, and Michael Unser, *Fellow, IEEE*

**Abstract**—We present a new family of two-dimensional and three-dimensional orthogonal wavelets which uses quincunx sampling. The orthogonal refinement filters have a simple analytical expression in the Fourier domain as a function of the order  $\lambda$ , which may be noninteger. We can also prove that they yield wavelet bases of  $L_2(\mathbb{R}^2)$  for any  $\lambda > 0$ . The wavelets are fractional in the sense that the approximation error at a given scale  $\alpha$  decays like  $O(\alpha^\lambda)$ ; they also essentially behave like fractional derivative operators. To make our construction practical, we propose a fast Fourier transform-based implementation that turns out to be surprisingly fast. In fact, our method is almost as efficient as the standard Mallat algorithm for separable wavelets.

**Index Terms**—McClellan transform, nonseparable filter design, quincunx sampling, wavelet transform.

## I. INTRODUCTION

THE GREAT majority of wavelet bases that are currently used for image processing are separable. There are two primary reasons for this. The first is convenience, because wavelet theory is most developed in one dimension and that these results are directly transposable to higher dimensions through the use of tensor product basis functions. The second is efficiency because a separable transform can be implemented by successive one-dimensional (1-D) processing of the rows and columns of the image. The downside, however, is that separable transforms tend to privilege the vertical and horizontal directions. They also produce a so-called “diagonal” wavelet component, which does not have a straightforward directional interpretation.

Nonseparable wavelets, by contrast, offer more freedom and can be better tuned to the characteristics of images [1], [2]. Their less attractive side is that they require more computations. The quincunx wavelets are especially interesting because they can be designed to be nearly isotropic [3]. In contrast with the separable case, there is a single wavelet and the scale reduction is more progressive: a factor  $\sqrt{2}$  instead of 2. The preferred technique for designing quincunx wavelets with good isotropy properties is to use the McClellan transform [4] to map 1-D biorthogonal designs to the multidimensional case. Since this approach requires the filters to be symmetric, it has only been applied to the biorthogonal case because of the strong incentive to produce filters that are compactly supported [5]–[8]. One

noteworthy exception is the work of Nicolier *et al.* who used the McClellan transform to produce a quincunx version of the Battle–Lemarié wavelet filters [9]. However, we believe that their filters were truncated because they used a representation in terms of Tchebycheff polynomials.

In this paper, we construct a new family of quincunx wavelets that are orthogonal and have a fractional order of approximation. The idea of fractional orders was introduced recently in the context of spline wavelets for extending the family to non-integer degrees [10]. The main advantage of having a continuously varying order parameter—not just integer steps as in the traditional wavelet families—is flexibility. It allows for a continuous adjustment of the key parameters of the transform, e.g., regularity and localization of the basis functions. The price that we are paying for these new features—orthogonality with symmetry as well as fractional orders—is that the filters can no longer be compactly supported. We will make up for this handicap by proposing a fast Fourier transform (FFT)-based implementation which is almost as efficient as Mallat’s algorithm for separable wavelets [11].

## II. QUINCUNX SAMPLING AND FILTERBANKS

First, we recall some basic results on quincunx sampling and perfect reconstruction filterbanks [12]. The quincunx sampling lattice is shown in Fig. 1. Let  $x[\vec{k}]$  with  $\vec{k} = (k_1, k_2) \in \mathbb{Z}^2$  denote the discrete signal on the initial grid. The two-dimensional (2-D)  $z$ -transform of  $x[\vec{k}]$  is denoted by  $X(\vec{z}) = \sum_{\vec{k} \in \mathbb{Z}^2} x[\vec{k}] \vec{z}^{-\vec{k}}$ , where  $\vec{z}^{\vec{k}} = z_1^{k_1} z_2^{k_2}$ . The continuous 2-D Fourier transform is then given by  $X(e^{j\vec{\omega}}) = \sum_{\vec{k} \in \mathbb{Z}^2} x[\vec{k}] e^{-j(\vec{\omega}, \vec{k})}$  with  $\vec{\omega} = (\omega_1, \omega_2)$ , and, finally, the discrete 2-D Fourier transform for  $x[\vec{k}]$  given on an  $N \times N$  grid  $(k_1, k_2 = 0, 1, \dots, N-1)$  by  $X[\vec{n}] = \sum_{\vec{k} \in \mathbb{Z}^2} x[\vec{k}] e^{-j2\pi(\vec{n}, \vec{k})/N}$ , with  $n_1, n_2 = 0, 1, \dots, N-1$ .

Now, we write the quincunx sampled version of  $x[\vec{k}]$  as

$$[x]_{1D}[\vec{k}] = x[\mathbf{D}\vec{k}], \quad \text{where } \mathbf{D} = \begin{pmatrix} 1 & 1 \\ 1 & -1 \end{pmatrix}. \quad (1)$$

Our down-sampling matrix  $\mathbf{D}$  is such that  $\mathbf{D}^2 = 2\mathbf{I}$ . The Fourier-domain version of (1) is

$$[x]_{1D}[\vec{k}] \longmapsto \frac{1}{2} \left[ X \left( e^{j\mathbf{D}^{-1}\vec{\omega}} \right) + X \left( e^{j(\mathbf{D}^{-1}\vec{\omega} + \vec{\pi})} \right) \right] \quad (2)$$

where  $\vec{\pi} = (\pi, \pi)$ .

The upsampling is defined by

$$[x]_{1D}[\vec{k}] = \begin{cases} x[\mathbf{D}^{-1}\vec{k}], & \text{when } k_1 + k_2 \text{ is even} \\ 0, & \text{elsewhere} \end{cases} \quad (3)$$

Manuscript received November 14, 2002; revised May 21, 2004. The associate editor coordinating the review of this manuscript and approving it for publication was Dr. Truong Q. Nguyen.

The authors are with the Biomedical Imaging Group, Swiss Federal Institute of Technology Lausanne (EPFL), CH-1015 Lausanne, Switzerland (e-mail: dimitri.vandeville@epfl.ch; michael.unser@epfl.ch)

Digital Object Identifier 10.1109/TIP.2005.843754

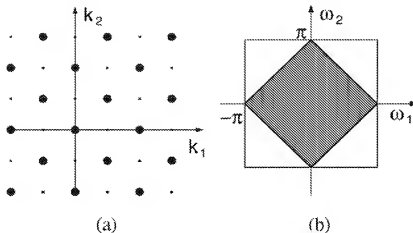


Fig. 1. (a) Quincunx lattice and (b) the corresponding Nyquist area in the frequency domain.

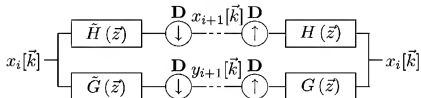


Fig. 2. Perfect reconstruction filterbank on a quincunx lattice.

and its effect in the Fourier domain is as follows:

$$[x]_{1D}[\vec{k}] \longleftrightarrow X(e^{j\vec{\omega}^T \vec{x}}). \quad (4)$$

If we now chain the down-sampling and up-sampling operators, we get

$$[x]_{1D1D}[\vec{k}] = \begin{cases} x[\vec{k}], & \text{when } k_1 + k_2 \text{ is even} \\ 0, & \text{elsewhere} \end{cases} \quad (5)$$

$$\frac{1}{2} [X(e^{j\vec{\omega}}) + X(e^{j(\vec{\omega} + \#)})]. \quad (6)$$

Since quincunx sampling reduces the number of image samples by a factor of two, the corresponding reconstruction filterbank has two channels (cf. Fig. 2). The low-pass filter  $\tilde{H}$  reduces the resolution by a factor of  $\sqrt{2}$ ; the wavelet coefficients correspond to the output of the high-pass filter  $\tilde{G}$ .

Applying the relation (6) to the block diagram in Fig. 2, it is easy to derive the conditions for a perfect reconstruction

$$\begin{cases} \tilde{H}(\vec{z})H(\vec{z}) + \tilde{G}(\vec{z})G(\vec{z}) = 2 \\ \tilde{H}(-\vec{z})H(\vec{z}) + \tilde{G}(-\vec{z})G(\vec{z}) = 0 \end{cases} \quad (7)$$

where  $H$  and  $G$  (respectively  $\tilde{H}$  and  $\tilde{G}$ ) are the transfer functions of the synthesis (respectively analysis) filters. In the orthogonal case, the analysis and synthesis filters are identical up to a central symmetry; the wavelet filter  $G$  is simply a modulated version of the low-pass filter  $H$ .

### III. FRACTIONAL QUINCUNX FILTERS

To generate quincunx filters, we will use the standard approach which is to apply the diamond McClellan transform to map a 1-D design onto the quincunx structure.

#### A. New 1-D Wavelet Family

As starting point for our construction, we introduce a new 1-D family of orthogonal filters

$$\begin{aligned} H_\lambda(z) &= \frac{\sqrt{2}(z+2+z^{-1})^{\frac{\lambda}{2}}}{\sqrt{(z+2+z^{-1})^\lambda + (-z+2-z^{-1})^\lambda}} \\ &= \frac{\sqrt{2}(2+2\cos\omega)^{\frac{\lambda}{2}}}{\sqrt{(2+2\cos\omega)^\lambda + (2-2\cos\omega)^\lambda}} \end{aligned} \quad (8)$$

which is indexed by the continuously-varying order parameter  $\lambda$ .

These filters are symmetric and are designed to have zeros of order  $\lambda$  at  $z = -1$ ; the numerator is a fractional power of  $(z+2+z^{-1})$  (the simplest symmetric refinement filter of order 2) and the denominator is the appropriate  $l_2$ -orthonormalization factor. By varying  $\lambda$ , we can adjust the frequency response as shown in Fig. 3. As  $\lambda$  increases,  $H_\lambda(z)$  converges to the ideal half-band low-pass filter. Also note that these filters are maximally flat at the origin; they essentially behave like  $H_\lambda(\omega)/\sqrt{2} = 1 + O(\omega^\lambda)$  as  $\omega \rightarrow 0$ . Their frequency response is similar to the Daubechies' filters with two important differences: 1) the filters are symmetric and 2) the order is not restricted to integer values.

We can prove mathematically that these filters will generate valid 1-D fractional wavelet bases of  $L_2$  similar to the fractional splines presented in [10]. The order property (here fractional) is essential because it determines the rate of decay of the approximation error as a function of the scale. It also conditions the behavior of the corresponding wavelet  $\psi$  which will act like a fractional derivative of order  $\lambda$ . In other words, it will kill all polynomials of degree  $n \leq \lceil \lambda - 1 \rceil$ ; i.e.

$$\int x^n \psi_\lambda(x) dx = 0. \quad (9)$$

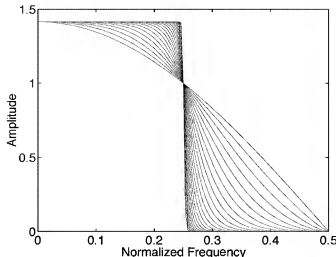


Fig. 3. Frequency responses of the orthogonal refinement filters for  $\lambda = 1, \dots, 100$ .

### B. Corresponding 2-D Wavelet Family

Applying the diamond McClellan transform to the filter above is straightforward; it amounts to replacing  $\cos \omega$  by  $(1/2)(\cos \omega_1 + \cos \omega_2)$  in (8). Thus, our quincunx refinement filter is given by

$$H_\lambda(e^{j\vec{\omega}}) = \frac{\sqrt{2}(2 + \cos \omega_1 + \cos \omega_2)^{\frac{\lambda}{2}}}{\sqrt{(2 + \cos \omega_1 + \cos \omega_2)^2 + (2 - \cos \omega_1 - \cos \omega_2)^2}^{\lambda}}. \quad (10)$$

This filter is guaranteed to be orthogonal because the McClellan transform has the property of preserving biorthogonality. Also, by construction, the  $\lambda$ th order zero at  $\omega = \pi$  gets mapped into a corresponding zero at  $\vec{\omega} = (\pi, \pi)$ ; this is precisely the condition that is required to get a 2-D wavelet transform of order  $\lambda$ . Also, note the isotropic behavior and the flatness of  $H_\lambda(e^{j\vec{\omega}})$  around the origin; i.e.,  $H_\lambda(e^{j\vec{\omega}})/\sqrt{2} = 1 + O(\|\vec{\omega}\|^\lambda)$  for  $\vec{\omega} \rightarrow 0$ . Fig. 4 shows contour plots of the scaling filter for several choices of the order  $\lambda$ .

The orthogonal wavelet filter is obtained by modulation

$$G_\lambda(\vec{x}) = z_1 H_\lambda(-\vec{x}^{-1}). \quad (11)$$

The corresponding orthogonal scaling function  $\varphi_\lambda(\vec{x})$  is defined implicitly as the solution of the quincunx two-scale relation

$$\varphi_\lambda(\vec{x}) = \sqrt{2} \sum_{\vec{k} \in \mathbb{Z}^2} h_\lambda(\vec{k}) \varphi_\lambda(\mathbf{D}\vec{x} - \vec{k}). \quad (12)$$

Since the refinement filter is orthogonal with respect to the quincunx lattice, it follows that  $\varphi_\lambda(\vec{x}) \in L_2(\mathbb{R}^2)$  and that it is orthogonal to its integer translates. Moreover, for  $\lambda > 0$ , it will satisfy the partition of unity condition, which comes as a direct consequence of the vanishing of the filter at  $(\omega_1, \omega_2) = (\pi, \pi)$ . Thus, we have the guarantee that our scheme will yield orthogonal wavelet bases of  $L_2(\mathbb{R}^2)$ . The underlying orthogonal quincunx wavelet is simply

$$\psi_\lambda(\vec{x}) = \sqrt{2} \sum_{\vec{k} \in \mathbb{Z}^2} g_\lambda(\vec{k}) \varphi_\lambda(\mathbf{D}\vec{x} - \vec{k}). \quad (13)$$

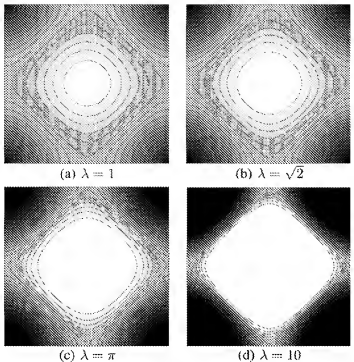


Fig. 4. Contour plots of the low-pass filters  $H_\lambda(e^{j\vec{\omega}})$  for various values of the order parameter  $\lambda$ . (a)  $\lambda = 1$ . (b)  $\lambda = \sqrt{2}$ . (c)  $\lambda = \pi$ . (d)  $\lambda = 10$ .

Given the behavior of  $H_\lambda(e^{j\vec{\omega}})$  at  $\vec{\omega} = 0$ , we also have  $\hat{\psi}_\lambda(\vec{\omega}) \propto \|\vec{\omega}\|^\lambda$ , and, as such, the wavelet behaves as the  $\lambda$ th order differentiator for low frequencies [13]. The vanishing moment property in the 2-D case becomes

$$\int x_1^{n_1} x_2^{n_2} \psi_\lambda(\vec{x}) d\vec{x}, \quad \text{for } n_1 + n_2 \leq \lceil \lambda - 1 \rceil. \quad (14)$$

Fig. 5 shows the wavelet  $\psi_\lambda(\vec{x})$  for various choices of the order  $\lambda$ . Also, note that the wavelet is centered around  $(1/2, 1/2)$ . As illustrated by these plots, the wavelets clearly gets smoother as  $\lambda$  increases. However, a mathematical rigorous estimation of their regularity is beyond the scope of this paper.

### IV. IMPLEMENTATION IN FOURIER DOMAIN

The major objection that can be made to our construction is that the filters are not FIR and that it may be difficult and costly to implement the transform in practice. We will see here that we can turn the situation around and obtain a very simple and efficient algorithm that is based on the IFFT, following the idea of [14]. Working in the frequency domain is also very convenient because of the way in which we have specified our filters [see (10) and (11)]. Implementations of the wavelet transform for the quincunx subsampling matrix using FFTs have been proposed before [9], [15]; our algorithm is another variation, which minimizes the number and size of FFTs and seems to be faster.

First, let us assume that the image size is  $N \times N$ . Now, we will describe the decomposition part of our algorithm which corresponds to the block diagram presented in Fig. 6, where we have pooled together two levels of the decomposition. The initialization step is to evaluate the FFT of the initial input image  $x[\vec{k}]$  and to precompute the corresponding sampled frequency responses

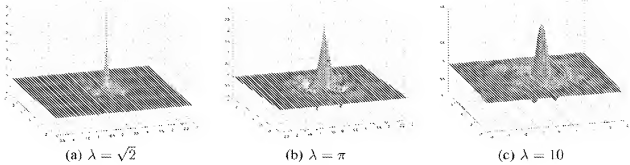


Fig. 5. Surface plots of the wavelets  $\psi_\lambda$  for various values of the order parameter. (a)  $\lambda = \sqrt{2}$ , (b)  $\lambda = \pi$ , (c)  $\lambda = 10$ .

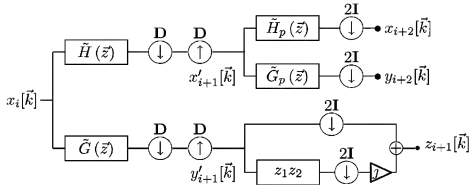


Fig. 6. Analysis part of the 2-D quincunx wavelet transform for two iterations.

of the analysis filters  $\tilde{H}[\vec{n}]$  and  $\tilde{G}[\vec{n}]$  using (10) and (11). We also precompute the rotated version of the filters, denoted as  $\tilde{H}_p[\vec{n}]$  and  $\tilde{G}_p[\vec{n}]$ , that can be obtained as

$$\tilde{H}_p[\vec{n}] = \tilde{H}[\mathbf{D}\vec{n} \bmod (N, N)] \quad (15)$$

$$\tilde{G}_p[\vec{n}] = \tilde{G}[\mathbf{D}\vec{n} \bmod (N, N)]. \quad (16)$$

Let us now consider the 2-D FFT of the input, given by

$$X_i[\vec{n}] = \sum_{\vec{k}} x_i[\vec{k}] e^{-j \frac{2\pi(\vec{k}, \vec{n})}{N}}, \quad \text{for } n_1, n_2 = 0, 1, \dots, N-1. \quad (17)$$

Globally, at the end of the process, the output variables are the quincunx wavelet coefficients  $y_1[\vec{k}], y_2[\vec{k}], \dots, y_J[\vec{k}]$ , and  $x_J[\vec{k}]$ ; e.g., as shown in Fig. 7(a). Their Fourier transforms for the odd iterations are derived from the auxiliary  $N \times N$  signals (see also Fig. 6)

$$X'_{i+1}[\vec{n}] = \sum_{\vec{k}} x'_{i+1}[\vec{k}] e^{-j \frac{2\pi(\vec{k}, \vec{n})}{N}} \quad (18)$$

$$Y'_{i+1}[\vec{n}] = \sum_{\vec{k}} y'_{i+1}[\vec{k}] e^{-j \frac{2\pi(\vec{k}, \vec{n})}{N}}. \quad (19)$$

Down and up sampling with  $\mathbf{D}$  in the first iteration step introduces zeros in the space domain while it preserves the size of  $Y'_{i+1}[\vec{n}]$ . However, it implies some symmetry/redundancy in frequency domain. Therefore, only half of the coefficients needs

to be computed which saves operations. The reduced signal  $Y'_{i+1}[\vec{n}']$  and its corresponding low-pass signal are obtained by

$$Y'_{i+1}[\vec{n}'] = \frac{1}{2} \left[ \tilde{G}[\vec{n}'] X_i[\vec{n}'] + \tilde{G}[\vec{n}' + \left( \frac{N}{2}, \frac{N}{2} \right)] X_i[\vec{n}' + \left( \frac{N}{2}, \frac{N}{2} \right)] \right] \quad (20)$$

$$X'_{i+1}[\vec{n}'] = \frac{1}{2} \left( \tilde{H}[\vec{n}'] X_i[\vec{n}'] + \tilde{H}[\vec{n}' + \left( \frac{N}{2}, \frac{N}{2} \right)] X_i[\vec{n}' + \left( \frac{N}{2}, \frac{N}{2} \right)] \right) \quad (21)$$

where  $\vec{n}' \in [0, (N/2) - 1] \times [0, N - 1]$ .

To generate the signal  $y_{i+1}[\vec{k}]$  of (19) in the way that is depicted in Fig. 7(a) with every second row shifted by one pixel, we separate the image in even ( $y_{i+1, \text{even}}$ ) and odd ( $y_{i+1, \text{odd}}$ ) rows already in the Fourier domain, using the auxiliary variable  $Z[\vec{m}]$

$$Z[\vec{m}] = Y'_{i+1}[\vec{m}] + Y'_{i+1} \left[ \vec{m} + \left( 0, \frac{N}{2} \right) \right] + j \left( Y'_{i+1}[\vec{m}] - Y'_{i+1} \left[ \vec{m} + \left( 0, \frac{N}{2} \right) \right] \right) e^{j \frac{2\pi(m_1 + m_2)}{N}} \quad (22)$$

$$z_{i+1}[\vec{k}] = y_{i+1, \text{even}}[\vec{k}] + j y_{i+1, \text{odd}}[\vec{k}] \quad (23)$$

with  $\vec{m} \in [0, (N/2) - 1]^2$ . The sum in the real part ( $Y'_{i+1}[\vec{m}] + Y'_{i+1}[\vec{m} + (0, N/2)]$ ) represents downsampling by two in the vertical direction, keeping all the even rows, whereas the sum

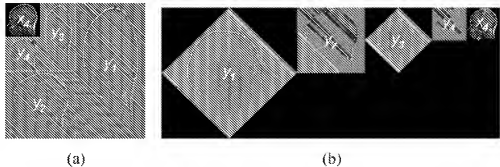


Fig. 7. Wavelet coefficients for the quincunx subsampling scheme can be arranged in two ways. An example for  $J = 4$  iterations. (a) Compact representation. (b) Classic representation.

in the imaginary part represents the odd rows. In the space domain, we alternate the rows  $y_{i+1}[k_1, 2k_2 + 1] = \text{Re}\{z[\vec{k}]\}$  and  $y_{i+1}[k_1, 2k_2] = \text{Im}\{z[\vec{k}]\}$ . Since  $z[\vec{k}]$  is four times smaller than  $y_{i+1}[\vec{k}]$ , we save computations with the reduced-size IFFT.

Instead of rotating the frequency variables after each iteration, we use the precomputed rotated version of the filters (i.e.,  $H_p$  and  $\tilde{G}_p$ ), which we apply at all even iterations. In this way, we also save two rotations per iteration in the frequency domain.

The Fourier transforms of the output for the even iterations are

$$Y_{i+2}[\vec{m}] = \sum_{\vec{k}} y_{i+2}[\vec{k}] e^{-j \frac{2\pi(\vec{k}, \vec{m})}{4}} \quad \text{for } m_1, m_2 = 0, 1, \dots, \frac{N}{2} - 1. \quad (24)$$

They are computed by

$$X_{i+2}[\vec{m}] = \frac{1}{2} \left( \tilde{H}_p[\vec{m}] X'_{i+1}[\vec{m}] + \tilde{H}_p \left[ \vec{m} + \left( 0, \frac{N}{2} \right) \right] \right. \\ \left. \times X'_{i+1} \left[ \vec{m} + \left( 0, \frac{N}{2} \right) \right] \right) \quad (25)$$

$$Y_{i+2}[\vec{m}] = \frac{1}{2} \left( \tilde{G}_p[\vec{m}] X'_{i+1}[\vec{m}] + \tilde{G}_p \left[ \vec{m} + \left( 0, \frac{N}{2} \right) \right] \right. \\ \left. \times X'_{i+1} \left[ \vec{m} + \left( 0, \frac{N}{2} \right) \right] \right). \quad (26)$$

The process is then iterated until one reaches the final resolution. When the last iteration is even, we lower the computation costs with the FFT by utilizing its imaginary part

$$z[\vec{k}] = \sum_{\vec{m}} (X_{i+2}[\vec{m}] + jY_{i+2}[\vec{m}]) e^{j \frac{2\pi(\vec{m}, \vec{k})}{4}} \quad (27)$$

where  $x_{i+2}[\vec{k}] = \text{Re}\{z[\vec{k}]\}$  and  $y_{i+2}[\vec{k}] = \text{Im}\{z[\vec{k}]\}$ .

Obviously, as the resolution gets coarser after each iteration, the Fourier transforms of the filters need not be recalculated; they are simply obtained by down-sampling the previous arrays.

The synthesis algorithm operates according to the same principles and corresponds to the flow graph transpose of the decom-

position algorithm using up sampling, instead. For instance, the synthesis counterpart of (25) and (26) is

$$X'_{i+2} \left[ m_1, m_2 + \left( \frac{N}{2} \right) \right] = X_{i+2}[m_1, m_2], \\ Y'_{i+2} \left[ m_1, m_2 + \left( \frac{N}{2} \right) \right] = Y_{i+2}[m_1, m_2], \\ X_{i+1}[m_1, m_2] = X'_{i+2}[m_1, m_2] H_p[m_1, m_2] \\ + Y'_{i+2}[m_1, m_2] G_p[m_1, m_2].$$

## V. EXPERIMENTS

### A. Benchmark and Testing

We have implemented two versions of the algorithm, based on Java and Matlab. For the Matlab version, we report computation times below 0.8 s for 16 quincunx iterations of a 256  $\times$  256 image on an Apple G4 700 MHz desktop; the decomposition is essentially perfect with a reconstruction error below  $10^{-12}$  RMS. The method is generic and works for any set of filters that can be specified in the frequency domain, independent of their spatial support (or infinite spatial support, such as in our case). As a comparison, the Matlab implementation available in the latest Wavelet Toolbox [16] for the Daubechies 9/7 filters (used in JPEG 2000) applied to the same image and for an equivalent of eight separable iterations, takes about 1.7 s. For  $N$  datapoints, the complexity of our approach boils down to  $\mathcal{O}(N \log N)$  for the FFT-based implementation, versus  $\mathcal{O}(NB)$  for the spatial-domain implementation, where  $B$  is related to the filter support. The exact tradeoff will depend on the image size and the filter size. However, taking into account the benchmark measures and its flexibility, we believe that the FFT-based implementation deserves consideration for a broad class of applications.

We also provide an applet written in Java, which makes it possible to run the algorithm over the Internet, at the site <http://bigwww.epfl.ch/demo/jquincunx/>. A screen shot of this applet is presented in Fig. 8.

Two examples of fractional quincunx wavelet decompositions with  $\lambda = \sqrt{2}$  and  $\lambda = \pi$  are shown in Fig. 9. Note how the residual image details are more visible for the lower value of  $\lambda$ . The larger  $\lambda$  reduces the energy of the wavelet coefficient, but this also comes at the expense of some ringing. Thus, it is

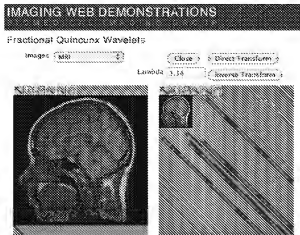


Fig. 8. Applet of the Fourier-based implementation of the quincunx wavelet transform, available on the site: <http://bigwww.epfl.ch/demo/jquincunx/>.

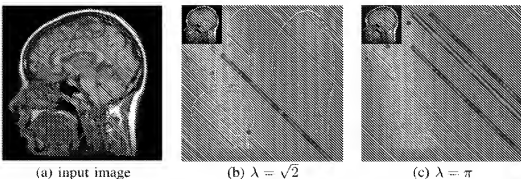


Fig. 9. Quincunx wavelet transforms with four iterations. (a) Original test image. (b)  $\lambda = \sqrt{2}$ . (c)  $\lambda = \pi$ .

convenient to have an adjustable parameter to search for the best tradeoff.

An advantage of the present approach is that the filters for small  $\lambda$  are nearly isotropic; this is the reason why the wavelet details in Fig. 9 do not present any preferential orientation. The degree of isotropy of the various lowpass filters can be seen from Fig. 4. The shape of the contour plots of the low-pass filter  $H_\lambda(e^{j\omega})$  confirms that the degree of isotropy is the best for small values of  $\lambda$ . At the other extreme, when  $\lambda \rightarrow \infty$ ,  $H_\lambda(e^{j\omega})$  tends to the diamond-shaped ideal filter.

Another nice feature of the algorithm is that the computational cost remains the same irrespective of the value of  $\lambda$ .

### B. Dependence of the Order Parameter

The usefulness of a tunable order parameter is demonstrated in the following experiment: we apply the quincunx transform to the test image "cameraman" [see Fig. 10(a)] and reconstruct using only 15% of the largest coefficients. Then the SNR is measured depending on the order parameter. The plot in Fig. 11 shows how the SNR changes according to the order  $\lambda$ ; the optimum, indicated by the circle, is achieved for  $\lambda = 2.5$ . Fig. 10(b) and (c) shows the reconstructions for the optimal order and an order too high. The last one gets penalized by the introduction of ringing artefacts around the edges. We also plot

the SNR curves for 20% and 25% of the coefficients. The same type of qualitative behavior holds for other images.

### C. Approximation Properties

The main differences between the quincunx and the conventional separable algorithm is the finer scale progression and the nonseparability. To test the impact that this may have on compression capability, we compared the approximation qualities of both approaches. Since the wavelet transform is orthogonal, the approximation error (distortion) is equal to  $D^2 = \|x - \hat{x}\|^2 = \|y - \hat{y}\|^2$ , where  $y$  are the wavelet coefficients of the input image  $x$ ;  $\hat{x}$  is the reconstructed image obtained from the quantized—or truncated—wavelet coefficients  $\hat{y}$ . Also,  $D^2$  in the space domain is equivalent to the sum of squares of discarded wavelet coefficients [17].

*1) Linear Approximation:* In classical rate-distortion theory, the coefficients are grouped into channels and coded independently. In the orthogonal case,  $D^2$  is equivalent to the difference between the signal's energy and the energy of the reconstructed signal  $\|x - \hat{x}\|^2 = \|x\|^2 - \|\hat{x}\|^2 = \|x\|^2 - (\|\hat{x}\|^2 + \sum_{j=1}^J \|\hat{y}_j\|^2)$ . The distortion across  $N$  channels with variance  $\sigma_i^2$  is

$$D = N \cdot C \cdot 2^{-2R} \cdot \rho^2 \quad (28)$$

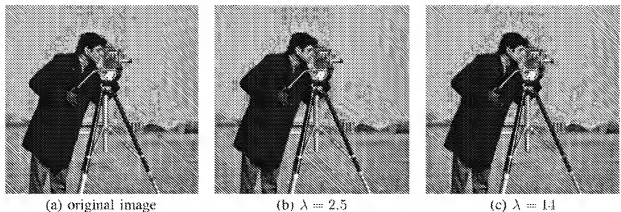


Fig. 10. (a) Original test image “cameraman.” (b) and (c) Reconstruction of “cameraman” using 15% of the largest coefficients with  $\lambda = 2.5$  (optimal) and  $\lambda = 1.4$ .

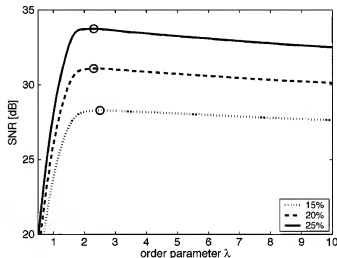


Fig. 11. Relation between the order parameter  $\lambda$  and the SNR of the reconstructed image (test image “cameraman”) using only the largest coefficients. The full line, dashed line, and dotted line correspond, respectively, to 15%, 20%, and 25% of the largest coefficients.

where  $C$  is a constant,  $\bar{R}$  is the mean rate, and  $\rho$  is the geometric mean of the subband variances

$$\rho = \left( \prod_{i=1}^N \sigma_i^2 \right)^{\frac{1}{N}}. \quad (29)$$

When  $\rho$  is small, the distortion is small, as well. What this means qualitatively is that the wavelet transform which has the larger spread in the variances will achieve the better coding gain [12]. The linear approximation subband coding gain for sample-by-sample quantization (PCM) is described by

$$G_{\text{PCM}} = \frac{D_{\text{PCM}}}{D_{\text{SBC}}} = \frac{\frac{1}{N} \sum_{i=1}^N \sigma_i^2}{\left( \prod_{i=1}^N \sigma_i^2 \right)^{\frac{1}{N}}}. \quad (30)$$

To better illustrate this issue, we have decomposed the test image “cameraman” for the maximal number of iterations, both for the quincunx and the separable case as shown in Fig. 12. The order was fixed (i.e.,  $\lambda = 4$ ) for our method and for the orthogonal separable approach (corresponding to the commonly

used degree parameter  $\alpha = 3$  for the underlying B-splines). In Fig. 13(a), we compare the energy packing properties of both decompositions for linear approximation. “Energy packing” refers to the property that the more the first coefficients contain energy, the better the DWT yields compression. We start to sum up the energy of the subbands with the lowest resolution. Each step of the stairs represents a subband.<sup>1</sup> The first subbands of the quincunx decomposition report higher energy packing than the separable case, but the overall coding gain is slightly better for the separable case than the quincunx case (47.69 versus 45.23). Fig. 13(c) shows similar results for the “Lena” test image.

Since the branches are orthogonal, the transformation that provides the maximum energy compaction in the low-pass channel is also the one that results in the minimum approximation error [17]. Since most images have a power spectrum that is roughly rotationally invariant and decreases with higher frequencies, separable systems are usually not best suited for isolating a low-pass channel containing most energy and having high-pass channels with low energy. In contrast, a quincunx low-pass filter will retain more of the original signal’s energy [12].

Consequently, the type of images that benefit the most from the quincunx scheme have a more isotropic spectrum. For example, for the well-known zoneplate test image of Fig. 14(a), the coding gain of quincunx scheme is about 20% better than the one obtained by the separable scheme (4.30 versus 3.64). Also, the quincunx scheme gives better energy compaction for textures of highly isotropic nature (and as such a higher coding gain). Two such examples of the Brodatz textures are shown in Fig. 14(b) and (c), corresponding to a coding gain of 13.67 versus 12.45 and 12.04 versus 9.62, respectively. On the other hand, a separable treatment leads to a better energy compaction for the texture shown in Fig. 15 (8.78 versus 15.48). Other authors have also found that texture analysis using the quincunx scheme improves the results as compared to the separable scheme [18].

<sup>1</sup>A quincunx wavelet decomposition with  $J$  iterations generates  $N = J + 1$  channels, while a separable wavelet decomposition with  $J$  iterations results into  $N = 3J + 1$  channels.

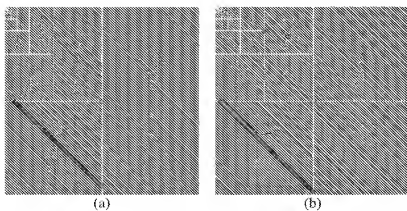


Fig. 12. Decomposition of the test image “cameraman” for the maximal possible number of iterations. (a) Quincunx case. (b) Separable case. The contrast of each subband has been enhanced.

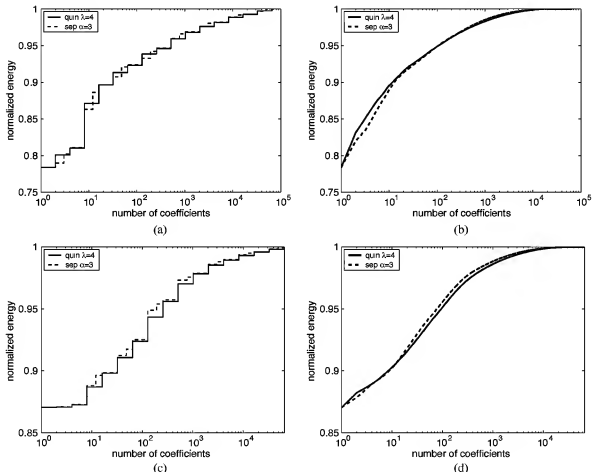


Fig. 13. Comparison of energy-compaction property between the quincunx and the separable case of image decomposition (as shown in Fig. 12). (a) and (c) Linear approximation depending on number of coefficients (in log, grouped per subband), respectively, for “cameraman” and “Lena.” (b) and (d) Nonlinear approximation depending of the  $n$  largest coefficients (in log), respectively, for “cameraman” and “Lena.” The quincunx scheme yields better results for a low number of coefficients. In the case of “Lena,” the separable scheme performs better than the quincunx one over most of the range.

2) *Nonlinear Approximation*: A more recent trend in wavelet theory is the study of *nonlinear approximation*. In this case we do not take the “ $n$ -first” coefficients, but the “ $n$ -largest” coefficients to approximate a signal with  $n$  coefficients. This yields better energy packing, since in the wavelet domain the “ $n$ -first” coefficients are not necessarily the largest one,

especially along the position indices [19]. The distortion is described by [20]

$$D^2 = \|y - y_{N(T)}\|^2 = \sum_{|y| < T} |y[n]|^2. \quad (31)$$

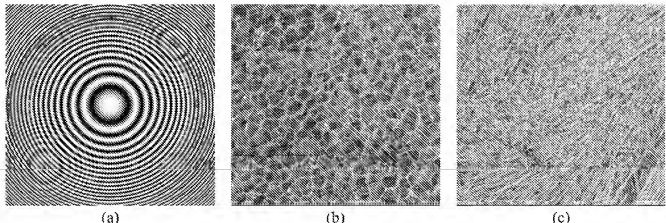


Fig. 14. Some examples of typical images where the quincunx scheme outperforms the separable case in term of coding gain. (a) Zoneplate. (b) Brodatz texture D112. (c) Brodatz texture D15. The Brodatz textures have  $512 \times 512$  pixels and are obtained from the USC-SIPI image database.

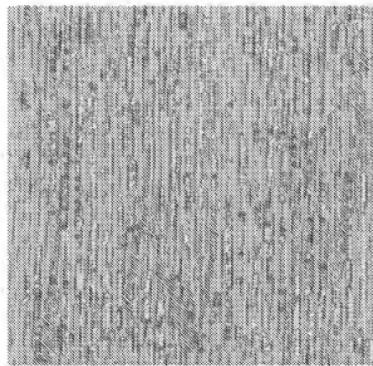


Fig. 15. Example of a texture (Brodatz D68) that is better suited for a separable treatment.

Moreover, it can be shown that

$$D \propto C \cdot (N(T))^{-\frac{2}{q}} \quad (32)$$

when the smoothness of  $y$  is measured by its inclusion in some critical Besov space  $B_q^\gamma(L^q(T))$  with  $1/q = (\gamma/2) + (1/2)$ , roughly speaking, when  $y$  is a function with  $\gamma$  derivatives in  $L^q(T)$  [20], [21].

For the nonlinear approximation, the quincunx scheme also yields a better approximation than the separable one for a small  $n$  in many cases. Fig. 13(b) represents the energy depending on the  $n$  largest coefficients (in log).

## VI. EXTENSION TO THREE DIMENSIONS

The extension of quincunx sampling to three dimensions is rather straightforward. First, the filters are obtained by replacing  $\cos \omega$  by  $(1/3)(\cos \omega_1 + \cos \omega_2 + \cos \omega_3)$  in (8). Next, the quincunx sampling lattice for three dimensions is shown in

Fig. 16(a). Let  $x[\vec{k}]$  denote the discrete signal on the initial grid. Then, its quincunx sampled version, following [6], is

$$[x]_{1D}[\vec{k}] = x[\mathbf{D}\vec{k}], \quad \text{where } \mathbf{D} = \begin{pmatrix} 1 & 0 & 1 \\ -1 & -1 & 1 \\ 0 & -1 & 0 \end{pmatrix}. \quad (33)$$

Our down-sampling matrix  $\mathbf{D}$  is such that  $\mathbf{D}^3 = 2\mathbf{I}$  and  $|\det \mathbf{D}| = 2$ . The Fourier-domain version of this formula is similar to the 2-D case

$$[x]_{1D}[\vec{k}] \longleftrightarrow \frac{1}{2} \left[ X(e^{j\mathbf{D}^{-T}\vec{\alpha}}) + X(e^{j(\mathbf{D}^{-T}\vec{\alpha} + \#)}) \right] \quad (34)$$

where  $\vec{\alpha} = (\pi, \pi, \pi)$ .

The implementation for the 3-D case goes as follows. The output variables are the discrete Fourier transforms of the wavelet coefficients

$$Y_{i+1}[\vec{n}] = \sum_{\vec{k}} y_{i+1}[\vec{k}] e^{-j\frac{2\pi(\vec{k}, \vec{n})}{N}} \quad \text{for } n_1, n_2, n_3 = 0, 1, \dots, N-1 \quad (35)$$

$$Y_{i+2}[\vec{n}] = \sum_{\vec{k}} y_{i+2}[\vec{k}] e^{-j\frac{2\pi(\vec{k}, \vec{n})}{N}} \quad \text{for } n_1, n_2, n_3 = 0, 1, \dots, N-1 \quad (36)$$

$$Y_{i+3}[\vec{m}] = \sum_{\vec{k}} y_{i+3}[\vec{k}] e^{-j\frac{2\pi(\vec{k}, \vec{m})}{N}} \quad \text{for } m_1, m_2, m_3 = 0, 1, \dots, \frac{N}{2}-1. \quad (37)$$

The coefficients themselves are recovered by inverse FFT. The Fourier transforms after the first level of filtering are given by

$$\begin{aligned} X_{i+1}[\vec{n}] &= \frac{1}{2} \left( \tilde{H}[\vec{n}] X_i[\vec{n}] + \tilde{H} \left[ \vec{n} + \left( \frac{N}{2}, \frac{N}{2}, \frac{N}{2} \right) \right] \right. \\ &\quad \left. \times X_i \left[ \vec{n} + \left( \frac{N}{2}, \frac{N}{2}, \frac{N}{2} \right) \right] \right) \end{aligned} \quad (38)$$

$$\begin{aligned} Y_{i+1}[\vec{n}] &= \frac{1}{2} \left( \tilde{G}[\vec{n}] X_i[\vec{n}] + \tilde{G} \left[ \vec{n} + \left( \frac{N}{2}, \frac{N}{2}, \frac{N}{2} \right) \right] \right. \\ &\quad \left. \times X_i \left[ \vec{n} + \left( \frac{N}{2}, \frac{N}{2}, \frac{N}{2} \right) \right] \right). \end{aligned} \quad (39)$$

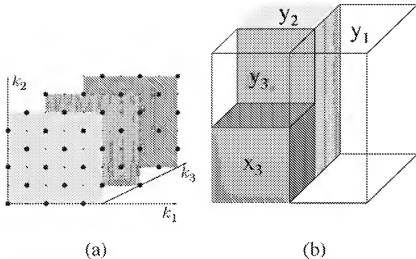


Fig. 16. (a) Three-dimensional (3-D) face-centered orthorhombic (FCO) lattice, corresponding to the sampling matrix of (33). (b) Compact representation of the wavelet coefficients for the 3-D case.

After the second level of filtering, we have

$$X_{i+2}[\vec{n}] = \frac{1}{2} \left( \tilde{H}_p[\vec{n}] X_{i+1}[\vec{n}] + \tilde{H}_p \left[ \vec{n} + \left( 0, \frac{N}{2}, 0 \right) \right] \right. \\ \left. \times X_{i+1} \left[ \vec{n} + \left( 0, \frac{N}{2}, 0 \right) \right] \right) \quad (40)$$

$$Y_{i+2}[\vec{n}] = \frac{1}{2} \left( \tilde{G}_p[\vec{n}] X_{i+1}[\vec{n}] + \tilde{G}_p \left[ \vec{n} + \left( 0, \frac{N}{2}, 0 \right) \right] \right. \\ \left. \times X_{i+1} \left[ \vec{n} + \left( 0, \frac{N}{2}, 0 \right) \right] \right). \quad (41)$$

Note that these are computed at the resolution of the input. The size reduction only takes place during the third step

$$X_{i+3}[\vec{m}] = \frac{1}{2} \left( \tilde{H}_{pp}[\vec{m}] X_{i+2}[\vec{m}] + \tilde{H}_{pp} \left[ \vec{m} + \left( \frac{N}{2}, 0, 0 \right) \right] \right. \\ \left. \times X_{i+2} \left[ \vec{m} + \left( \frac{N}{2}, 0, 0 \right) \right] \right) \quad (42)$$

$$Y_{i+3}[\vec{m}] = \frac{1}{2} \left( \tilde{G}_{pp}[\vec{m}] X_{i+2}[\vec{m}] + \tilde{G}_{pp} \left[ \vec{m} + \left( \frac{N}{2}, 0, 0 \right) \right] \right. \\ \left. \times X_{i+2} \left[ \vec{m} + \left( \frac{N}{2}, 0, 0 \right) \right] \right) \quad (43)$$

where  $\tilde{H}_p[\vec{m}] = \tilde{H}[\mathbf{D}\vec{m} \bmod (N, N, N)]$  and  $\tilde{H}_{pp}[\vec{m}] = \tilde{H}[\mathbf{D}^2\vec{m} \bmod (N, N, N)]$ . Analogously, we have that:  $\tilde{G}_p[\vec{m}] = \tilde{G}[\mathbf{D}\vec{m} \bmod (N, N, N)]$  and  $\tilde{G}_{pp}[\vec{m}] = \tilde{G}[\mathbf{D}^2\vec{m} \bmod (N, N, N)]$ .

Fig. 16(b) shows how the coefficients can be arranged in a nonredundant way inside the cube. Note that the size of the FFTs for the 3-D implementation can be further reduced by taking into account the subsampled arrangement in the Fourier domain. Again, the rotated filters  $H_p$ ,  $H_{pp}$ ,  $G_p$ , and  $G_{pp}$  are precomputed.

#### A. Approximation Properties in Three Dimensions

We compared the compression capability for the quincunx and the separable scheme applied to 3-D data, similar to the type of experiments that are described for two dimensions in Section V-C. Fig. 17 shows the results for a spiral CT dataset of part of a human spine. The linear approximation quality is shown in Fig. 17(b). The separable scheme takes much advantage of the availability of many small (i.e., seven for each iteration) bandpass subbands, as compared to the quincunx scheme. To illustrate this point, we have grouped the bandpass subbands for the separable case together in one single bandpass in Fig. 17(c). For nonlinear approximation, both schemes perform similarly with a small advantage for the separable one, as shown in Fig. 17(d). If the dataset contains more (isotropic) high-frequency components, the breakpoint between the quincunx and the separable case shifts to the right.

The main advantage of the 3-D quincunx scheme is in applications that can benefit from the (much) slower scale progression. One example is the statistical analysis of brain activity using functional magnetic resonance imaging (fMRI). Here we show an example using the classical wavelet-based approach for detecting activity, using the linear model analysis and the *t* test in the wavelet domain for a 3-D dataset ( $64 \times 64 \times 64$ ) with an auditory stimulus [22]; we refer to [23] for more details. We compared the use of the 3-D dyadic separable wavelet decomposition based on orthogonal linear B-spline wavelets versus our 3-D quincunx wavelets (same order). The parameter maps where obtained using the same threshold after reconstruction (5% of the maximal parameter value). The number of detected voxels, and as such the sensitivity of the approach, is almost 10% higher (578 versus 536) when we use the 3-D quincunx DWT, which confirms that the slower scale progression improves the quality of the results. Fig. 18 shows the detected activation patterns around the auditory cortex (slice 33).

Other potential applications might include image analysis and 3-D feature detection.

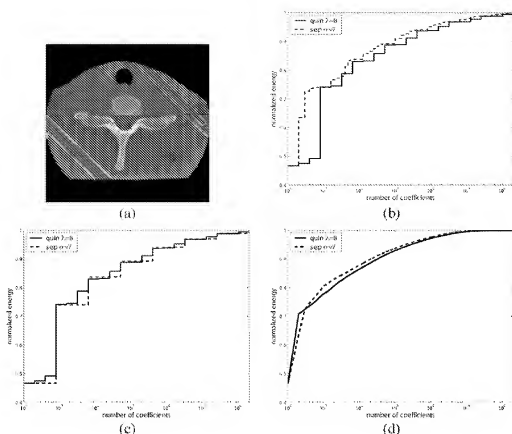


Fig. 17. (a) Slice of an spiral CT dataset of part of a human spine (courtesy and copyright of Ramanu Pichumani, Stanford University School of Medicine). (b) Linear approximation, for the separable case each bandpass subband is considered independently. (c) Linear approximation, for the nonseparable case the bandpass subbands are grouped together into one single subband. (d) Nonlinear approximation.

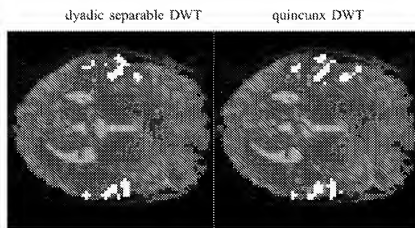


Fig. 18. FMRI brain activation detected using the classical wavelet based approach. The activated voxels in the slice are left white, superposed on a background of the T2\* scan.

## VII. CONCLUSION

We have introduced a new family of orthogonal wavelet transforms for quincunx lattices. A key feature is the continuously varying order parameter  $\lambda$  which can be used to adjust the bandpass characteristics as well as the localization of the basis functions.

We have also demonstrated that these wavelet transforms could be computed quite efficiently in two and three dimensions

using FFTs. This should help dispel the commonly held belief that nonseparable wavelet decompositions are computationally much more demanding than the separable ones.

Because of their nice properties and their ease of implementation, these wavelets present an alternative to the separable ones that are being used in a variety of image processing applications (image analysis, image enhancement, filtering and denoising, feature detection, texture analysis, and so on).

## REFERENCES

[1] J. Kovačević and M. Vetterli, "Nonseparable two- and three-dimensional wavelets," *IEEE Trans. Signal Process.*, vol. 43, no. 5, pp. 1269–1273, May 1995.

[2] A. Mojsilović, M. Popović, S. Marković, and M. Krstić, "Characterization of visually similar diffuse diseases from B-scan liver images using nonseparable wavelet transform," *IEEE Trans. Med. Imag.*, vol. 17, no. 4, pp. 541–549, Apr. 1998.

[3] J. C. Feauveau, "Analyse multirésolution avec un facteur de résolution  $\sqrt{2}$ ," *J. Traitement du Signal*, vol. 7, no. 2, pp. 117–128, 1990.

[4] J. H. McClellan, "The design of two-dimensional digital filters by transformations," in *Proc. 7th Annu. Princeton Conf. Information Sciences and Systems*, Princeton, NJ, 1973, pp. 247–251.

[5] A. Cohen and I. Daubechies, "Nonseparable bidimensional wavelet bases," *Rev. Mat. Iberoamericana*, vol. 9, pp. 51–137, 1993.

[6] J. Kovačević and M. Vetterli, "Nonseparable multidimensional perfect reconstruction filter banks and wavelet bases for  $\mathbb{R}^n$ ," *IEEE Trans. Inf. Theory*, vol. 38, no. 2, pp. 533–555, Mar. 1992.

[7] J. Shapiro, "Adaptive McClellan transformations for quincunx filter banks," *IEEE Trans. Signal Process.*, vol. 42, no. 3, pp. 642–648, Mar. 1994.

[8] D. B. H. Tay and N. G. Kingsbury, "Flexible design of multidimensional perfect reconstruction FIR 2-band filters using transformations of variables," *IEEE Trans. Image Process.*, vol. 2, no. 4, pp. 466–480, Apr. 1993.

[9] F. Nicolier, O. Laligant, and F. Truchetet, "B-spline quincunx wavelet transform and implementation in Fourier domain," *Proc. SPIE*, vol. 3522, pp. 223–234, Nov. 1998.

[10] M. Unser and T. Blu, "Fractional splines and wavelets," *SIAM Rev.*, vol. 42, pp. 43–67, 2000.

[11] S. Mallat, "A theory for multiresolution signal decomposition: the wavelet representation," *IEEE Trans. Pattern Anal. Mach. Intell.*, vol. 11, no. 4, pp. 674–693, Apr. PAMI-1989.

[12] M. Vetterli and J. Kovačević, *Wavelets and Subband Coding*. Upper Saddle River, NJ: Prentice-Hall, 1995.

[13] M. Unser and T. Blu, "Fractional wavelets, derivatives, and Besov spaces," in *Proc. SPIE Conf. Mathematical Imaging: Wavelet Applications in Signal and Image Processing X*, vol. 5207, San Diego, CA, Aug. 2003, pp. 147–152.

[14] O. Rioul and P. Duhamel, "Fast algorithms for discrete and continuous wavelet transforms," *IEEE Trans. Signal Process.*, vol. 38, no. 2, pp. 569–586, Mar. 1992.

[15] F. Nicolier, O. Laligant, and F. Truchetet, "Discrete wavelet transform implementation in Fourier domain for multidimensional signal," *J. Electron. Imag.*, vol. 11, no. 3, pp. 338–346, Jul. 2002.

[16] *Wavelet Toolbox 2.2*. Natick, MA: Mathworks, Inc., 2000.

[17] M. Unser, "On the optimality of ideal filters for pyramid and wavelet signal approximation," *IEEE Trans. Signal Process.*, vol. 41, no. 12, pp. 3591–3596, Dec. 1993.

[18] F. Nicolier, A. Legrand, O. Laligant, S. Kohler, and F. Truchetet, "Oocyte texture analysis through almost shift-invariant decimated wavelet transform," in *Proc. 4th Int. Conf. Knowledge-Based Intelligent Engineering Systems & Allied Technologies*, Brighton, U.K., Aug. 2000, pp. 385–388.

[19] D. L. Donoho, M. Vetterli, R. A. DeVore, and I. Daubechies, "Data compression and harmonic analysis," *IEEE Trans. Inf. Theory*, vol. 44, no. 6, pp. 2435–2475, Nov. 1998.

[20] R. A. DeVore, B. Jawerth, and B. J. Lucier, "Image compression through wavelet transform coding," *IEEE Trans. Inf. Theory*, vol. 38, no. 2, pp. 719–746, Mar. 1992.

[21] R. A. DeVore, "Nonlinear approximation," *Acta Numer.*, vol. 7, pp. 51–150, 1998.

[22] Single subject epoch (block) auditory fMRI activation data, G. Rees and K. Friston. (1999). [Online]. Available: <http://www.fil.ion.ucl.ac.uk/spm/data/>

[23] D. Van De Ville, T. Blu, and M. Unser, "Wavelets versus resels in the context of fMRI: establishing the link with SPM," in *Proc. SPIE Symp. Optical Science and Technology: Wavelets X*, vol. 5207, Aug. 2003, pp. 417–425.



**Manuela Feilner** was born in Zürich, Switzerland, in 1973. She graduated in electronic engineering from the Swiss Federal Institute of Technology Zürich (ETHZ), Zürich, and received the Ph.D. degree in statistical wavelet analysis of functional images of the brain from the Biomedical Imaging Group, Swiss Federal Institute of Technology Lausanne (EPFL), Lausanne, Switzerland, in 1998 and 2002, respectively.



**Dimitri Van De Ville** (M'02) was born in Dendermonde, Belgium, in 1975. He received the Engineering Degree in Computer Science and the Ph.D. degree from Ghent University, Ghent, Belgium, in 1998 and 2002, respectively.

During his Ph.D. studies, he was a Research Assistant with the Fund for Scientific Research, Flanders, Belgium, where he was also a member of the Medical Image and Signal Processing Group (MEDISIP) and the MultiMedia Laboratory, Department of Electronics and Information Systems (ELIS). His Ph.D. research included resampling techniques for image and video processing. He is now with the Biomedical Imaging Group, Swiss Federal Institute of Technology Lausanne (EPFL), Lausanne, Switzerland. His current research interests include splines, wavelets, approximation and sampling theory, and biomedical signal and imaging applications, such as fMRI and microscopy imaging.

Dr. Van De Ville is currently an Associate Editor for the IEEE SIGNAL PROCESSING LETTERS.



**Michael Unser** (M'89-SM'94-F'99) received the M.S. (*summa cum laude*) and Ph.D. degrees in electrical engineering from the Swiss Federal Institute of Technology Lausanne (EPFL), Lausanne, Switzerland, in 1981 and 1984, respectively.

From 1985 to 1997, he was with the Biomedical Engineering and Instrumentation Program, National Institutes of Health, Bethesda, MD, where he headed the Image Processing Group. He is now Professor and Director of the Biomedical Imaging Group, EPFL. His research area is biomedical image processing. He has a strong interest in sampling theories, multiresolution algorithms, wavelets, and the use of splines for image processing, and he is the author of over 100 published journal papers in these areas.

Dr. Unser is the Associate Editor-in-Chief of the IEEE TRANSACTIONS ON MEDICAL IMAGING. He has acted as Associate Editor or member of the editorial boards for the IEEE SIGNAL PROCESSING MAGAZINE, the IEEE TRANSACTIONS ON IMAGE PROCESSING (1992 to 1995), and the IEEE SIGNAL PROCESSING LETTERS (1994 to 1998). He was general Co-Chair for the first IEEE International Symposium on Biomedical Imaging (ISBI'2002), Washington, DC, July 7–10, 2002. He received the 1995 and 2003 Best Paper Awards and the 2000 Magazine Award from the IEEE Signal Processing Society.

# On the Multidimensional Extension of the Quincunx Subsampling Matrix

Dimitri Van De Ville, *Member, IEEE*, Thierry Blu, *Member, IEEE*, and Michael Unser, *Fellow, IEEE*

**Abstract**—The dilation matrix associated with the three-dimensional (3-D) face-centered cubic (FCC) sublattice is often considered to be the natural 3-D extension of the two-dimensional (2-D) quincunx dilation matrix. However, we demonstrate that both dilation matrices are of different nature: while the 2-D quincunx matrix is a similarity transform, the 3-D FCC matrix is not. More generally, we show that it is impossible to obtain a dilation matrix that is a similarity transform and performs downsampling of the Cartesian lattice by a factor of two in more than two dimensions. Furthermore, we observe that the popular 3-D FCC subsampling scheme alternates between three different lattices: Cartesian, FCC, and quincunx. The latter one provides a less isotropic sampling density, a property that should be taken into account to properly orient 3-D data before processing using such a subsampling matrix.

**Index Terms**—Nonseparable design, two-channel filterbanks, wavelet decomposition, 2-D quincunx sampling, 3-D FCC sampling.

## I. INTRODUCTION

THE QUINCUNX sampling scheme is an interesting configuration that is commonly used for designing critically sampled filterbanks and discrete wavelet transforms in two dimensions [1]–[7]. In contrast to the dyadic separable case, the quincunx dilation matrix leads to a two-channel filterbank architecture—or equivalently one single wavelet—and reduces the scale more progressively: a factor  $\sqrt{2}$  instead of 2. We briefly review the two-dimensional (2-D) quincunx scheme in Section II.

The growing availability of three-dimensional (3-D) volumetric and spatio-temporal data increases the interest for 3-D two-channel designs. The dilation matrix associated to the 3-D face-centered cubic (FCC) sublattice is often proposed as the natural extension of the 2-D quincunx case [7]–[9]. However, we point out a fundamental difference between the 2-D quincunx and the 3-D FCC matrices: the 3-D FCC matrix does not correspond to a similarity transform (i.e., an angle-preserving transformation such as rotation or symmetry combined with dilation) as does the 2-D quincunx matrix. Moreover, we show that, for more than two dimensions, it is impossible to find a dilation matrix on the Cartesian lattice that is a similarity transform and at the same time leads to a two-channel filterbank. Consequently, when the 3-D FCC dilation matrix is cascaded, the Voronoi cells of the sublattices are not just obtained by a simple

rotation/symmetry and dilation. In particular, for the 3-D FCC case, we observe an alternation between three types of lattices: Cartesian, FCC, and quincunx in the  $x - z$  plane. This observation can be useful to guide the orientation of the 3-D data before processing. These results are discussed in Section III.

## II. TWO-DIMENSIONAL QUINCUNX SUBSAMPLING

We characterize the Cartesian lattice by its sites  $\mathbf{k} = [k_1 \ k_2]^T$ ,  $k_1, k_2 \in \mathbb{Z}$ . An admissible  $2 \times 2$  dilation matrix  $\mathbf{D}$ , mapping  $\mathbf{k}$  to  $\mathbf{D}\mathbf{k}$ , must satisfy the following properties [10], [11]:

- 1) The new lattice forms a sublattice of the Cartesian lattice; a trivial property when each element of  $\mathbf{D}$  is integer.
- 2) The magnitude of each eigenvalue  $\lambda_i$  of  $\mathbf{D}$  must be strictly larger than 1 to ensure a dilation in each dimension.

After applying the dilation matrix, the density of the lattices sites is reduced by a factor  $|\det \mathbf{D}|$ . The Voronoi cell of the lattice is defined as the set of points closer to the origin than to any other lattice site, and completely characterizes the lattice's geometric structure [12]. The dual or reciprocal lattice is characterized by the matrix that is the transpose of the inverse dilation matrix; the reciprocal lattice serves in the frequency domain to replicate the spectrum while its Voronoi cell can be considered as the Nyquist region [8], [13].

The quincunx sublattice consists of those lattices sites  $[k_1 \ k_2]^T$ , where  $k_1 + k_2 = 2n$ ,  $n$  integer. There are two common choices for the corresponding dilation matrix:

$$\mathbf{D}_1 = \begin{bmatrix} 1 & 1 \\ 1 & -1 \end{bmatrix}, \quad \mathbf{D}_2 = \begin{bmatrix} 1 & -1 \\ 1 & 1 \end{bmatrix}. \quad (1)$$

Note that both matrices correspond to a similarity transform; i.e., a symmetry ( $\mathbf{D}_1$ ) or a rotation ( $\mathbf{D}_2$ ), combined with a dilation that reduces the number of sites by a factor of two ( $|\det \mathbf{D}_1| = |\det \mathbf{D}_2| = 2$ ). For signal processing applications, an interesting property is to have the iterated sublattice coincide again with a dilated Cartesian lattice after a few iterations. This property also contributes to the construction of smooth wavelets [14]. For these examples, we have  $\mathbf{D}_1^2 = 2\mathbf{I}$  and  $\mathbf{D}_2^2 = 16\mathbf{I}$ .

The design of orthogonal filters for quincunx sampling is strongly determined by the shape of the Voronoi cell of the reciprocal sampling lattice. More specifically, the goal is to design an orthogonal filter whose frequency response is reasonably close to the ideal filter characterized by the indicator function of the Nyquist region of the sampling lattice in the frequency domain, which corresponds to the Voronoi cell of the reciprocal lattice. Some filter and wavelet design examples can be found in [5], [7], [10], and [15]–[19].

Manuscript received May 27, 2004; revised July 8, 2004. The associate editor coordinating the review of this manuscript and approving it for publication was Dr. Xiang-Gen Xia.

The authors are with the Biomedical Imaging Group (BIG), Swiss Federal Institute of Technology Lausanne (EPFL), Lausanne CH-1015, Switzerland. Digital Object Identifier 10.1109/LSP.2004.839697

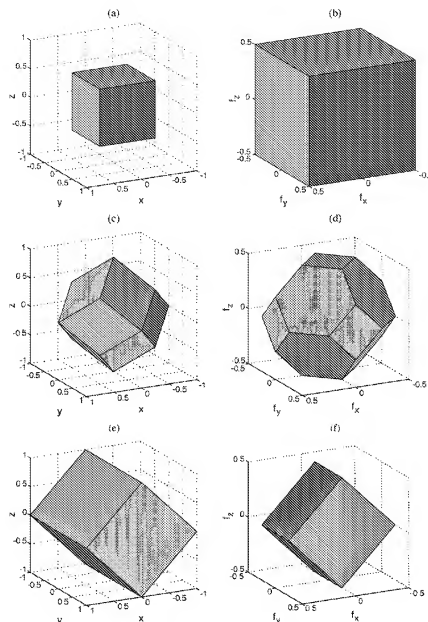


Fig. 1. Types of 3-D lattices encountered when the 3-D FCC dilation matrix is iterated. Left column: the Voronoi cell of the lattice in the spatial domain for the lattices (a)  $\mathbf{D}^0 \mathbf{k}$ , (c)  $\mathbf{D}^1 \mathbf{k}$ , (e)  $\mathbf{D}^2 \mathbf{k}$  (notice that the side in the  $x - z$  plane have length  $\sqrt{2}$ , while the sides in the  $y$  direction have length 2). Right column: the Voronoi cell of the reciprocal lattice in the frequency domain for the lattices (b)  $(\mathbf{D}^{-T})^0 \mathbf{k}$ , (d)  $(\mathbf{D}^{-T})^1 \mathbf{k}$ , (f)  $(\mathbf{D}^{-T})^2 \mathbf{k}$ . (a) Cartesian lattice; (b) cartesian lattice; (c) FCC lattice; (d) BCC lattice; (e) quincunx lattice  $x - z$ ; (f) quincunx lattice  $f_x - f_z$ .

Since the 2-D quincunx matrix corresponds to a similarity transform, its associated Voronoi cell in the spatial and the frequency domain is simply rotated or mirrored and dilated. Therefore, iterating  $\mathbf{D}_1$  and  $\mathbf{D}_2$  alternates between a Cartesian and a quincunx sublattice.

### III. THREE-DIMENSIONAL FCC SUBSAMPLING

The dilation matrix corresponding to the 3-D FCC sublattice is often considered to be the natural extension of the 2-D quincunx scheme. The corresponding most popular dilation matrix (cf. [4], [8], [10], and [20]) is

$$\mathbf{D} = \begin{bmatrix} 1 & 0 & 1 \\ -1 & -1 & 1 \\ 0 & -1 & 0 \end{bmatrix}. \quad (2)$$

It leads to a two-channel design ( $|\det \mathbf{D}| = 2$ ) and coincides with a dilated Cartesian lattice after three iterations; i.e., we have  $\mathbf{D}^3 = 2\mathbf{I}$ .

The use of the FCC sampling scheme is motivated by the energy packing argument [21]. Indeed, together with the body-centered cubic (BCC) lattice, the FCC lattice has the densest lattice packing in 3-D: it retains a maximal energy proportion for signals with a spherical spectrum.<sup>1</sup> Therefore, as in the 2-D case, the shape of the frequency response of an orthogonally designed filter on the FCC lattice tends to the indicator function

<sup>1</sup>In signal processing literature, the term face-centered orthorhombic (FCO) is often used instead of FCC. However, the FCO lattice allows for a scaling along the coordinate axes and therefore the argument of maximal energy compaction for signals with a spherical spectrum is no longer valid. Since the scaling is rarely used, we prefer the use of the term FCC.

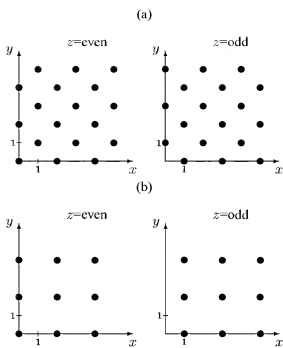


Fig. 2. Two-dimensional cuts of the 3-D lattices obtained by iterating the 3-D FCC dilation. (a)  $Dk$ . (b)  $D^2k$ .

TABLE I  
PROPERTIES OF THE ITERATED 3-D FCC MATRIX OF (2)

iteration	spatial lattice	reciprocal lattice	sampling density
$3n$	Cartesian lattice	Cartesian lattice	$2^{3n}(1, 1, 1)$
$3n + 1$	FCC lattice	BCC lattice	$2^{3n}(\sqrt[3]{2}, \sqrt[3]{2}, \sqrt[3]{2})$
$3n + 2$	Quincunx ( $x-z$ )	Quincunx ( $f_x-f_z$ )	$2^{3n}(\sqrt{2}, 2, \sqrt{2})$

of the Voronoi cell of the BCC lattice, which is a space-filling polyhedron that fills the space in an optimal way for signals with a spherical spectrum. Some examples of 3-D filter design can be found in [10], [17], [19], [20], and [22]–[24].

However, there is a fundamental difference between the 2-D quincunx and the 3-D FCC dilation matrix. The latter does not correspond to a similarity transform. More generally, we can show the following.

*Proposition 1:* For dimensions greater than 2, no dilation matrix can be a similarity matrix with determinant 2.

*Proof:* Assume that  $D$  is an admissible dilation matrix in  $N$  dimensions that corresponds to a similarity transform. Then it should satisfy

$$D^T D = mI, \quad (3)$$

where  $m$  is an integer. Taking the determinant of (3) gives

$$|\det D| = \sqrt{m^N}. \quad (4)$$

On the other hand, by the two-channel design constraint, we need

$$|\det D| = 2. \quad (5)$$

Satisfying both constraints (4) and (5) would require

$$m = \sqrt[3]{4} \quad (6)$$

with  $m$  integer, which is only possible for  $N = 2$ . ■

Now we know that no 3-D dilation matrix with determinant 2 exists that corresponds to a similarity transform. Nevertheless, it is interesting to take a closer look at the popular 3-D FCC matrix (2) and the consequences of not having this property. For this purpose, we determine the Voronoi cell at each iteration for both the spatial and the dual lattice [12], [21]. Since we have  $D^3 = 2I$ , the iterated scheme alternates between three lattices, but due to the lack of being a similarity transform, with fundamentally different Voronoi cells. For  $D^{3n}$ ,  $n \in \mathbb{N}$ , we have the Cartesian lattice and the corresponding cubic Voronoi cell in the spatial and the frequency domain, see Fig. 1(a) and (b). For  $D^{3n+1}$ , we have the FCC lattice in the spatial domain [Fig. 1(c)] where the Voronoi cell is a rhombic dodecahedron, and the BCC lattice in the frequency domain [Fig. 1(d)] where the Voronoi cell is a truncated octahedron. Finally, for  $D^{3n+2}$ , we obtain a quincunx sublattice in the  $x-z$  plane, while the  $y$  dimension is already subsampled by 2; see Fig. 1(e) and (f), respectively. Logically, the Voronoi cell of the spatial domain gets larger when the lattice gets coarser, while the inverse happens for the dual lattice. The lattices are also illustrated by 2-D cuts in Fig. 2. The alternation between those lattices is summarized in Table I and has two important consequences. First, the optimal energy packing argument for orthogonal filter design is only valid for one of the three lattices. Second, the quincunx arrangement for each third lattice  $D^{3n+2}$  has a less isotropic sampling density, which also influences orthogonally designed filters. Applications can use this property to properly adapt the orientation of 3-D data before treatment; e.g., for spatio-temporal data, the temporal direction could be put along the  $y$ -axis.

#### IV. CONCLUSION

The 3-D FCC dilation matrix is often considered to be the natural extension of the 2-D quincunx case. However, the dilation matrices have a different nature. In this paper, we have shown that the popular 3-D FCC dilation matrix, as opposed to the 2-D quincunx matrix, does not correspond to a similarity transform. Moreover, for more than two dimensions, it is impossible to build a two-channel dilation matrix on the Cartesian lattice which corresponds to a similarity transform. Still, the 3-D FCC dilation matrix can be useful to treat 3-D volumetric or spatiotemporal data. However, one should be aware that iterating the dilation matrix produces an alternation between lattices with a different degree of isotropy; i.e., Cartesian, FCC, and quincunx lattices.

#### REFERENCES

- [1] M. Vetterli, "Multi-dimensional sub-band coding: some theory and algorithms," *Signal Process.*, vol. 6, no. 2, pp. 97–112, 1984.
- [2] R. Ansari, H. Gaglio, and D. J. LeGall, "HDTV coding using a nonrectangular subband decomposition," *Proc. SPIE Conf. Visual Signal Commun. Image Process.*, Cambridge, MA, 1988, pp. 821–824.
- [3] J.-C. Feauveau, "Analyse multirésolution par ondelettes non orthogonales et bancs de filtres numériques," Ph.D. dissertation, Univ. Paris Sud, Paris, France, 1990.
- [4] M. Vetterli, J. Kováčević, and D. J. LeGall, "Perfect reconstruction FIR filter banks: some properties and factorizations," *Image Commun.*, vol. 2, no. 3, pp. 349–364, 1990.

- [5] E. Visciari and J. P. Allebach, "The analysis and design of multidimensional FIR perfect reconstruction filter banks for arbitrary sampling lattices," *IEEE Trans. Circuits Syst.*, vol. 38, no. 1, pp. 29–42, Jan. 1991.
- [6] A. Cohen and I. Daubechies, "Non-separable bidimensional wavelet bases," *Revista Matematica Iberoamericana*, vol. 9, pp. 51–137, 1993.
- [7] J. Kovacević and W. Sweldens, "Wavelet families of increasing order in arbitrary dimensions," *IEEE Trans. Image Process.*, vol. 9, no. 3, pp. 480–496, Mar. 2000.
- [8] E. Dubois, "The sampling and reconstruction of time-varying imagery with application in video systems," *Proc. IEEE*, vol. 73, no. 4, pp. 502–522, Apr. 1985.
- [9] P. Dafas, I. Kompassiari, and M. G. Strintzis, *Advances in Geometric Modeling*, Chichester, U.K.: Wiley Europe, 2003, ch. Optimal Hierarchical Adaptive Mesh Construction Using FCO Sampling.
- [10] J. Kovacević and M. Vetterli, "Nonseparable multidimensional perfect reconstruction filter banks and wavelet bases for  $\mathbb{R}^n$ ," *IEEE Trans. Inform. Theory*, vol. 38, no. 2, pp. 533–555, Mar. 1992.
- [11] K. Gröchenig and W. R. Madych, "Multiresolution analysis, Haar bases and self-similar tilings of  $\mathbb{R}^n$ ," *IEEE Trans. Inform. Theory*, vol. 38, no. 2, pp. 556–568, Mar. 1992.
- [12] E. Viterbo and E. Biglieri, "Computing the Voronoi cell of a lattice: the diamond-cutting algorithm," *IEEE Trans. Inform. Theory*, vol. 42, no. 1, pp. 161–171, Jan. 1996.
- [13] D. P. Petersen and D. Middleton, "Sampling and reconstruction of wave-number-limited functions in  $N$ -dimensional Euclidean spaces," *Inform. Contr.*, vol. 5, pp. 279–323, 1962.
- [14] K. Gröchenig and A. Ron, "Tight compactly supported wavelet frames of arbitrarily high regularity," *Proc. Amer. Math. Soc.*, no. 126, pp. 1101–1107, 1998.
- [15] R. H. Bammerger and M. J. T. Smith, "A filter bank for the directional decomposition of images: theory and design," *IEEE Trans. Signal Process.*, vol. 40, no. 4, pp. 882–893, Apr. 1992.
- [16] T. Chen and P. P. Vaidyanathan, "Multidimensional multirate filters and filter banks derived from one-dimensional filters," *IEEE Trans. Signal Process.*, vol. 41, no. 5, pp. 1749–1765, May 1993.
- [17] J. Kovacević and M. Vetterli, "Nonseparable two- and three-dimensional wavelets," *IEEE Trans. Signal Process.*, vol. 43, no. 5, pp. 1269–1273, May 1995.
- [18] K. S. C. Pun and T. Q. Nguyen, "A novel and efficient design of multidimensional PR two-channel filter banks with hourglass-shaped passband support," *IEEE Signal Process. Lett.*, vol. 11, no. 3, pp. 345–348, Mar. 2004.
- [19] M. Feilner, D. Van De Ville, and M. Unser, "An orthogonal family of quincunx wavelets with continuously-adjustable order," *IEEE Trans. Image Process.*, to be published.
- [20] J. Kovacević and M. Vetterli, "FCO sampling of digital video using perfect reconstruction filter banks," *IEEE Trans. Image Process.*, vol. 2, no. 1, pp. 118–122, Jan. 1993.
- [21] J. H. Conway and N. J. A. Sloane, *Sphere Packings, Lattices, and Groups*, 2nd ed., New York: Springer-Verlag, 1993.
- [22] D. B. H. Tay and N. G. Kingsbury, "Design of nonseparable 3-D filter banks/wavelet bases using transformations of variables," *Proc. Inst. Elect. Eng.—Vision Image Signal Process.*, vol. 143, no. 1, pp. 51–61, 1996.
- [23] D. B. H. Tay, "Analytical design of 3-D wavelet filter banks using the multivariate Bernstein polynomial," *Proc. Inst. Elect. Eng.—Vision Image Signal Process.*, vol. 147, no. 2, pp. 122–130, 2000.
- [24] ———, "Parametric Bernstein polynomial for least squares design of 3-D wavelet filter banks," *IEEE Trans. Circuits Syst. I*, vol. 49, no. 6, pp. 887–891, Jun. 2002.